Thermodynamic Origin of Nonvolatility in Resistive Memory

Jingxian Li[1], Anirudh Appachar[1], Sabrina L. Peczonczyk[2], Elisa T. Harrison[2], Anton V. Ievlev[3], Ryan Hood[4], Dongjae Shin[1], Sangmin Yoo[5], Brianna Roest[1], Kai Sun[1], Karsten Beckmann[6,7], Olya Popova[3], Tony Chiang[1], William S. Wahby[8], Robin B. Jacobs-Godrim[8], Matthew J. Marinella[9], Petro Maksymovych[3], John T. Heron[1,10], Nathaniel Cady[6], Wei D. Lu[5], Suhas Kumar[4], A. Alec Talin[4], Wenhao Sun[1,10], Yiyang Li[1,10 †]

[1]Materials Science and Engineering, University of Michigan, Ann Arbor, MI, 48109, USA

[2]Ford Research, Dearborn, MI, 48124 USA

[3]Center for Nanophase Materials Science, Oak Ridge National Laboratory,
Oak Ridge, TN, 37831, USA

[4]Sandia National Laboratories, Livermore, CA,94550, USA

[5]Electrical Engineering and Computer Science, University of Michigan, Ann Arbor, MI, 48109, USA

[6]College of Nanotechnology, Science and Engineering, University at Albany, NY, 12203, USA

[7]NY CREATES, Albany, NY, 12203 USA

[8]Sandia National Laboratories, Albuquerque, NM, 87123, USA

[9]Electrical, Computer, and Energy Engineering, Arizona State University, AZ, 85281, USA

[10]Applied Physics Program, University of Michigan, MI, 48109, USA

Corresponding author: yiyangli@umich.edu

[†] Lead Contact: yiyangli@umich.edu

Summary

Electronic switches based on the migration of high-density point defects, or memristors, are poised to revolutionize post-digital electronics. Despite significant research, key mechanisms for filament formation and oxygen transport remain unresolved, hindering our ability to predict and design device properties. For example, experiments have achieved 10 orders of magnitude longer retention times than predicted by current models. Here, using electrical measurements, scanning probe microscopy, and first-principles calculations on tantalum oxide memristors, we reveal that the formation and stability of conductive filaments crucially depend on the thermodynamic stability of the amorphous oxygen-rich and oxygen-poor compounds, which undergo composition phase separation. Including the previously neglected effects of this amorphous phase separation reconciles unexplained discrepancies in retention and enables predictive design of key performance indicators such as retention stability. This result emphasizes non-ideal thermodynamic interactions as key design criteria in post-digital devices with defect densities substantially exceeding those of today's covalent semiconductors.

Main Text

The success of modern electronics depends in large part on the ability to precisely control intrinsic and extrinsic point defects[1]. In covalent semiconductors like silicon, point defect concentrations are generally low, which results in them following Fick's first law of diffusion for ideal solutions ($J = -D\,\nabla c$). On the other hand, many emerging technologies such as ferroelectrics[2], hybrid perovskites[3], correlated oxides[4], and 2D materials[5] often contain substantially higher point defect concentrations (>1%). In such materials, the effects of nonideal interactions such as phase separation on defect transport cannot be ignored.

Resistive random access memory (RRAM)[6–10], or memristor, is a promising nonvolatile memory that utilizes exceptionally high point defect concentrations (>10%). With fast switching, high density, and long retention, RRAM has attracted substantial interest in information storage[7], in-memory computing[8], and neuromorphic computing[9]. Filament-type valence change memories (VCM)[6] are the most well-studied RRAM. In these VCM, an applied voltage induces the movement of oxygen ions (vacancies) to form or break a conducting filament, changing the tunnel distance at the Schottky barrier, and changing the resistance state[11,12].

The ideal diffusion equation $J = -D\,\nabla c$, which assumes that defects are noninteracting and follow ideal solution thermodynamics, has been universally used to describe oxygen diffusion in VCM[14–18,22–24]. Under no applied voltages, Fig. 1a schematically illustrates the most direct application of ideal Fickian diffusion to a bilayer VCM, whereby oxygen vacancies diffuse from the oxygen-deficient conductive reservoir into the initially insulating (near-)stoichiometric switching oxide. Because this bilayer mixing model predicts that pristine devices would become conducting and therefore fail after fabrication[25], it is not used to model retention. Instead, it is generally assumed that oxygen vacancies do not migrate between the stoichiometric and suboxide layers during retention[13–17]. This modified ideal diffusion model predicts that oxygen vacancies diffuse out of the high-concentration filament (Fig. 1b), resulting in a dissolution of the (broken) filament and a slow change from the LRS and HRS to a more resistive state over time, and is consistent with some experiments[14,18].

Although this modified ideal diffusion model is commonly used to describe oxygen transport in VCM, there are substantial unexplained inconsistencies with experimental data on tantalum oxide VCM. First, when using experimentally-derived diffusion constants for tantalum oxide[25,26], this model underestimates the measured retention time by 5-10 orders of magnitude[14,27]. Second, while this model predicts filament dissolution, experimental measurements have shown evidence for both higher resistance from filament dissolution[14,15,18,19] (Fig. 1b) and lower resistance from filament strengthening[15,16,20,28] (Fig. 1c). Filament strengthening and the associated decrease in resistance cannot be predicted using ideal Fickian diffusion. Despite decades of research, there is no physical explanation for these substantial deviations in both magnitude and direction from ideal diffusion in VCM.

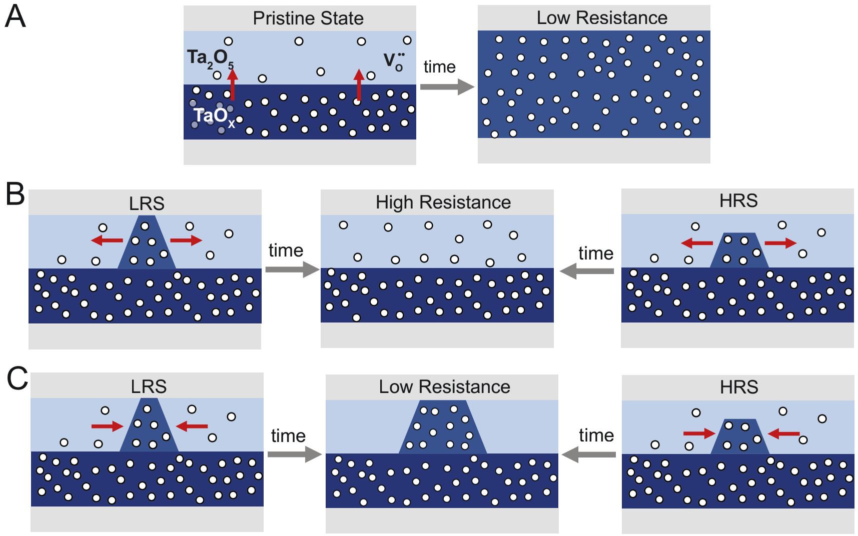

Fig. 1 Schematic of potential oxygen vacancy migration pathways under no applied voltage in bilayer TaOx VCM. a) Fick's first law for ideal solutions, which states that mobile species diffuse from high to low concentration, suggests that the Ta_2O_5 will rapidly gain oxygen vacancies when in contact with a suboxide, resulting in failure shortly after fabrication. **b)** Most models assume that oxygen vacancies do not migrate between the two oxide layers during retention[13–17]. Under this diffusion model, the filament dissolves, resulting in increased resistance over time, a result consistent with some experiments[14,18,19]. **c)** Other experiments suggest that the filament strengthens over time, yielding a decrease in resistance[15,20,21]. This result cannot be explained by either the ideal solution Fickian diffusion model, and represents a knowledge gap. We propose this behavior results from phase separation.

In this work, we show that the universally accepted Fickian diffusion model based on ideal solution thermodynamics is inadequate for describing mass transport in VCM. Instead, it is important to not only consider entropic interactions as in ideal solutions, but also consider the enthalpic effects of composition phase separation into amorphous oxygen-rich and oxygen-deficient phases, which can be modeled using the Cahn-Hilliard equation[29]. By combining novel experimental and computational methods with established techniques, we show that oxygen vacancies do not necessarily migrate from high to low concentrations. Rather, oxygen transport follows the gradient of the oxygen chemical potential of the amorphous compounds, where the filaments may strengthen under certain compositions. Our work corrects a longstanding yet inaccurate assumption of ideal Fickian diffusion as it applies to VCM, and shows that information retention, the core function of nonvolatile memory, has a thermodynamic origin and is not only a result of slow oxygen diffusion. We further propose and experimentally validate a thermodynamic design rule based on the gradient energy penalty for resistive memory that will undergo retention failure. More broadly, these results show the importance of accounting for defect interactions and phase separation in new classes of electronic materials.

Results

Retention Measurements in TaO_X-based VCM

We assess retention behavior under different annealing (baking) temperatures and times. Because no driving voltages are applied, retention studies eliminate the convoluting factors of electric field and temperature gradients. Our bilayer VCM consists of ~4 nm near-stoichiometric Ta_2O_5 above a ~30 nm sub-stoichiometric $TaO_{0.5}$ suboxide (see Experimental Procedures for fabrication details). X-ray diffraction and transmission electron microscopy show that both tantalum (sub-)oxide layers are amorphous due to the low deposition temperatures (Fig. S1). In Fig. 2a, our devices show the ability to switch between the low resistance state (LRS, ~1,000 μS) and high resistance state (HRS, 10-100 μS). Fig. S2 shows the switching statistics.

After confirming the switching characteristics, we annealed the devices at different temperatures in inert Ar, quenched to below 100°C in under 2 minutes, and measured the device conductance at room temperature. We define failure as when the conductance crosses 500 μS. We first consider pristine devices: after baking for 24 hours at 250°C, the conductance increases, but remains substantially more insulating than either the LRS or HRS, and does not fail (Fig. 2b). Because the devices remain insulating, it does not follow the bilayer mixing pathway illustrated in Fig. 1a even at this comparatively high temperature.

Next, we assess the devices starting in the LRS, where the conductance does not decrease over time as predicted by the widely-used modified Fickian pathway (Fig. 1b). Instead, the conductance increases. This stability is consistent with filament strengthening as depicted schematically in Fig. 1c. Additionally, none of the LRS or pristine devices annealed at temperatures below 350^{o}C fails (Fig. S3). We next consider HRS retention. At 250^{o}C, most HRS devices fail within 24 hours, reverting to a higher-conducting state (Fig. 2b). A statistical significance test comparing LRS and HRS failure shows a Z-value >3 (Note S1). This HRS failure indicates oxygen vacancies diffuse into the filament gap, which decreases the tunnel gap at the Schottky barrier between the oxide and the high work function Pd electrode[30]. In Fig. 2c, we quantify the fraction of HRS devices that fail (>500 μS), and show that the failure time increases at lower temperatures, consistent with previous work[15,18,27]. The stability of the pristine sample shows the reversion to the LRS is not a result of bilayer mixing. Moreover, devices annealed in air also show the same results (Fig. S3b), confirming that HRS retention failure is not a result of environmental reduction. While there exists significant device-to-device variability, all HRS devices showed a substantial increase in conductance across every temperature tested. Unfortunately, the devices could no longer switch after annealing. This may result from a slight reduction of the Ta_2O_5 layer upon heating, and could be seen with the increase in the conductance of the "pristine" devices upon annealing (Fig. 2b).

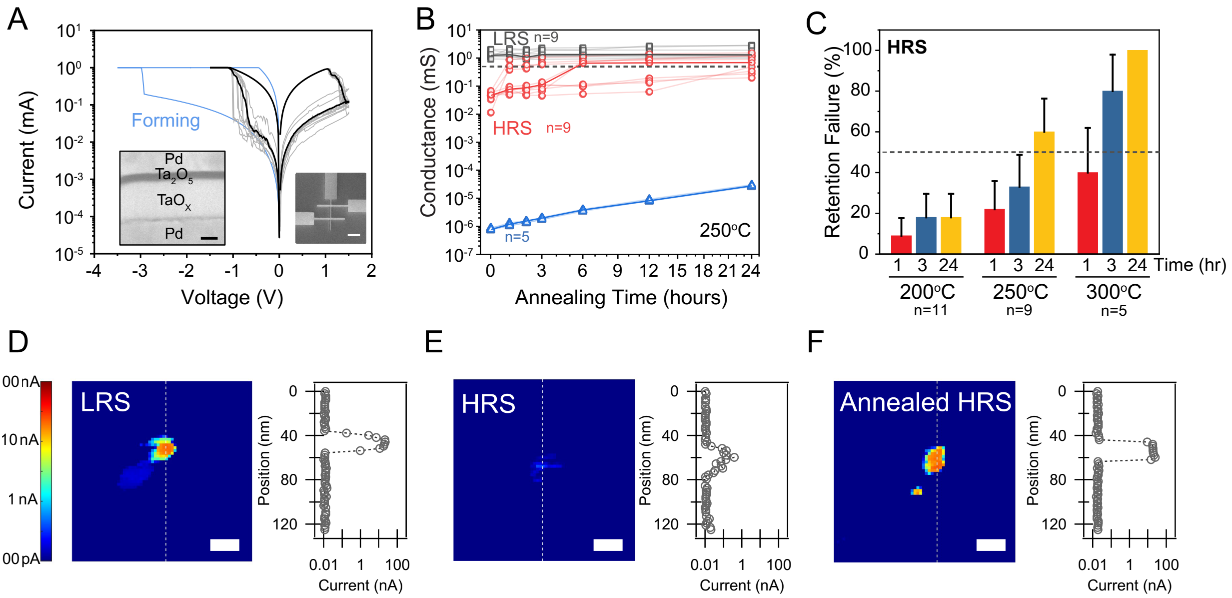

Fig. 2 Switching, retention, and conductive AFM characterization of the bilayer TaO_X-based memristors. a) A typical switching curve from the ~2 μm^2 crossbar device shows typical resistive switching behavior. The inserts show cross-section TEM (left, 10 nm scale bar) and planar SEM image (right, 10 μm scale bar) **b)** Retention characteristics of devices from the pristine state, HRS, and LRS baked at 250 ^{o}C. LRS and pristine state devices are stable, while HRS devices fail over time. The grey dashed line represents the failure threshold. n is the number of devices measured in each condition. **c)** HRS retention failure statistics show accelerated device failure as the bake temperature increases. The error bar represents one standard deviation for a binomial distribution (fail or not fail). **d-f)** C-AFM of the conductive filaments in devices with LRS device (d), HRS device (e), and HRS device annealed at 300^{o}C for 3 hours (f). The broken HRS filament re-forms after annealing in (f). Scale bar is 20 nm.

We use conductive atomic force microscopy (c-AFM) to visualize filament changes. Rather than using the AFM tip to switch the device, we electrically SET or RESET the device to the desired state (Fig. 2a), then use an Ar ion beam to remove the top contact. This ensures that we measure the filaments that exist under standard electrical forming and switching conditions, as opposed to filaments made using an AFM tip. Under a 0.5 V bias, our results show an ~8 nm filament with a peak current of ~20 nA in the LRS device (Fig. 2d), a much weaker filament (~1 nA) in the HRS device (Fig. 2e), and the re-emergence of the filament in an annealed HRS device (Fig. 2f). Importantly, the ~10-100× lower c-AFM current in the HRS device is consistent with the ~20× ON/OFF ratio in the devices. More c-AFM results are given in Fig. S4, which also shows the topology and currents of all imaged devices; no filaments were observed in the pristine devices which were not cycled (Fig. S4). The absence of filaments in the pristine, unformed samples (Fig. S4a,b) shows that the imaged filaments (Fig. 2d-f) were not created by the Ar ion beam; however, we cannot rule out possible surface damage by the Ar ion beam on the underlying oxide layer.

Our results in this section show that both the LRS and the pristine devices are stable for >24 hours at 200-350^{o}C. The HRS, on the other hand, fails; c-AFM measurements show this failure results from the re-formation of the nanoscale filament. Combined, these results show that the filaments revert from a nonequilibrium, frozen-in state after switching to a stable state with an intact filament and low device resistance after annealing. These observations are inconsistent with either Fickian diffusion pathways (Fig. 1a,b). We will later explain these differences in the context of phase separation, which can explain why some experiments show HRS retention failure[15,16,20,21] like ours, while others yield LRS retention failure[14,18,19].

Oxygen tracer diffusion in TaO$_X$

To gain further insight into the mechanism for HRS retention failure, we approximate the retention time using the characteristic oxygen (vacancy) diffusion time[14,15,31]. The Arrhenius activation energy (E_A) plays the largest role in determining diffusion time. Our HRS results, as well as previous literature results, suggest that the retention (diffusion) time can be modeled using E_A~1.5 eV (Fig. S5). However, direct oxygen diffusion measurements of Ta_2O_5 show that E_A ranges between 0.8 and 1.2 eV[23,32], which predicts ~5-12 orders of magnitude faster oxygen diffusion and shorter device retention times[23,26,32].

We hypothesize that oxygen diffusion in tantalum sub-oxides is much slower and has higher activation energy compared to Ta_2O_5. Whereas the retention time is determined by the oxygen diffusivity of the TaO_X sub-oxides that make up the filament, past results only quantified diffusion in the oxidized Ta_2O_5. To test our hypothesis, we quantified oxygen tracer diffusion in Ta (sub)-oxides using trilayer structures that consist of $Ta^{16}O_X/Ta^{18}O_X/Ta^{16}O_X$ (X~0.7, 1.5, 2.5). The isotope-enriched center layer is formed using $^{18}O_2$-enriched gas in the reactive sputtering gas mixture (Fig. 3a, S6), as recently conducted for amorphous HfO_2[33]. We then anneal these structures and use Time-of-Flight, Secondary Ion Mass Spectrometry (ToF-SIMS) to determine the $^{18}O/^{16}O$ ratio as a function of depth. Directly incorporating the tracer ^{18}O into the film enables tracer diffusion measurements in highly reduced sub-oxides, which cannot be accessed in standard gas-phase isotope exchange.

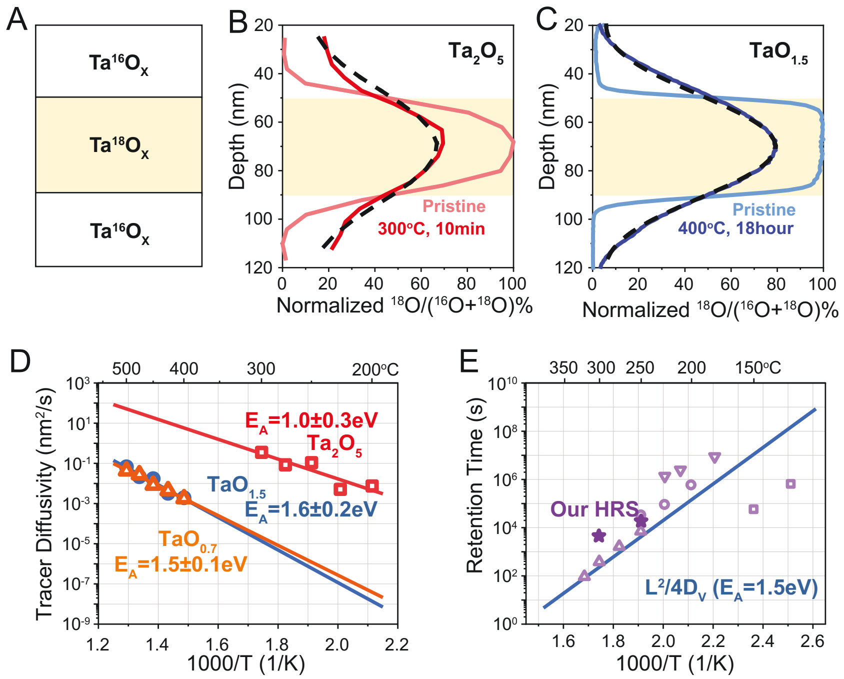

Fig. 3 Diffusion kinetics of TaO_X with ToF-SIMS and effects on retention failure. a) We develop a trilayer sample structure that embeds the ^{18}O tracer into the film stack, eliminating gas-phase reaction and enabling suboxide tracer diffusion measurements. **b-c)** Tracer diffusion results of Ta_2O_5 (b) and $TaO_{1.5}$ (c) trilayer samples. Black dotted line shows the fitted Fourier series solution to the diffusion equation. Sub-oxide $TaO_{1.5}$ shows much slower diffusivity compared with that of oxidized Ta_2O_5. **d)** Fitted activation energy of oxygen tracer diffusivity in TaO_X. Ta_2O_5 shows ~0.5 eV lower activation energy (E_A) than that of sub-oxides. The uncertainty indicates 1 standard error. **e)** Comparison of characteristic diffusion time with the vacancy diffusivity estimated from the tracer diffusion activation energy in ToF-SIMS experiments (blue line) with experimental retention times (dark purple star). The diffusion time activation energy of sub-stoichiometric oxides also matches well with retention time of TaO_X devices from literature (light purple symbols), where each symbol represents a different paper[15,18,27,34].

In Figs. 3b and c, we show oxygen tracer diffusion profiles for the oxidized Ta_2O_5 and the $TaO_{1.5}$ sub-oxide, respectively. While the Ta_2O_5 film shows substantial tracer diffusion after just 10 minutes at 300°C, the sub-oxide requires over 18 hours at 400°C to observe a similar tracer concentration profile. Our results yield a tracer diffusion activation energy of 1.0±0.3 eV for the amorphous Ta_2O_5 film, and between 1.5±0.2 and 1.6±0.2 eV for the two sub-oxides $TaO_{0.7}$ and

$TaO_{1.5}$ (Fig. 3d, see all fits in Fig. S7). This reduction in diffusivity with higher oxygen vacancy concentration has also been observed in $SrTiO_3$[35].

The much slower oxygen diffusivity in the sub-oxides explains the excellent retention time. In Fig. 3e, we show that the retention time activation energy for the unstable state, HRS in our case, is ~1.5 eV, consistent with the higher ~1.5 eV activation energy of the sub-oxide. However, our stable state (LRS) has even longer retention and does not appear to fail. As we will explain next, this remarkable stability cannot be explained only by oxygen diffusion rates.

Composition phase separation in amorphous Ta-O system

Our observation of increased conductance of both LRS and HRS during retention (Fig. 2) suggests that oxygen (vacancies) may diffuse against the concentration gradient (Fig. 1a); this "uphill diffusion" commonly arises during compositional phase separation[29]. In our experiments, phase separation describes the coexistence of two compositionally distinct materials with no net mass flux between the two layers, or "flux equilibrium" where $J=0$ (see Note S2). Here, the two phases are both amorphous with different Ta:O ratios[36]. Although these amorphous compounds are metastable and have higher energy than the inaccessible crystalline states, mass transport follows the chemical potential of the amorphous states when the crystalline states are inaccessible below 600^{o}C[37]. While phase transformations have been studied in tantalum oxide memristors[38–40], their relationship to retention time has not been previously considered.

The combination of amorphous materials and the highly variable nanosized filaments make it difficult to probe the effects of phase separation on oxygen transport in a filaments. Instead of probing nanosized filaments, we construct a bilayer film with different metal to oxygen ratios as a model system to assess compositional phase separation. X-ray photoelectron spectroscopy results by Heisig et al.[41] showed that the chemistry of a filament is nearly identical to that of a directly sputtered suboxide. Additionally, TEM studies show that the filament is also amorphous[42]. Building on these results, we anticipate a sputtered amorphous suboxide will have similar thermodynamics as an amorphous oxygen-deficient filament[36].

We fabricate bilayer films using a ~35 nm stoichiometric Ta_2O_5 layer on top of ~45 nm tantalum sub-oxides TaO_X with different compositions (X) to investigate phase separation over time. We first investigate the $TaO_{0.7}$ sub-oxide (~60 at% Ta). After annealing the sample at 300^{o}C for 3 hours, the top Ta_2O_5 layer reduces to $TaO_{1.9}$ (~35 at% Ta), while the bottom sub-oxide remains $TaO_{0.7}$ (Fig. 4a). The compositional interface between the two layers persists, but moves in position to conserve mass. Importantly, samples annealed at 16 and 48 hours show essentially identical depth profiles (Fig. 4a). Under the premise that the crystalline state is kinetically unattainable at this temperature[37], our results show that these amorphous samples have reached a state of "flux equilibrium" (J=0) in less than 3 hours. This state shows that composition phase separation is the favored configuration; in contrast, Fick's First Law would predict a progression to a homogeneous single phase.

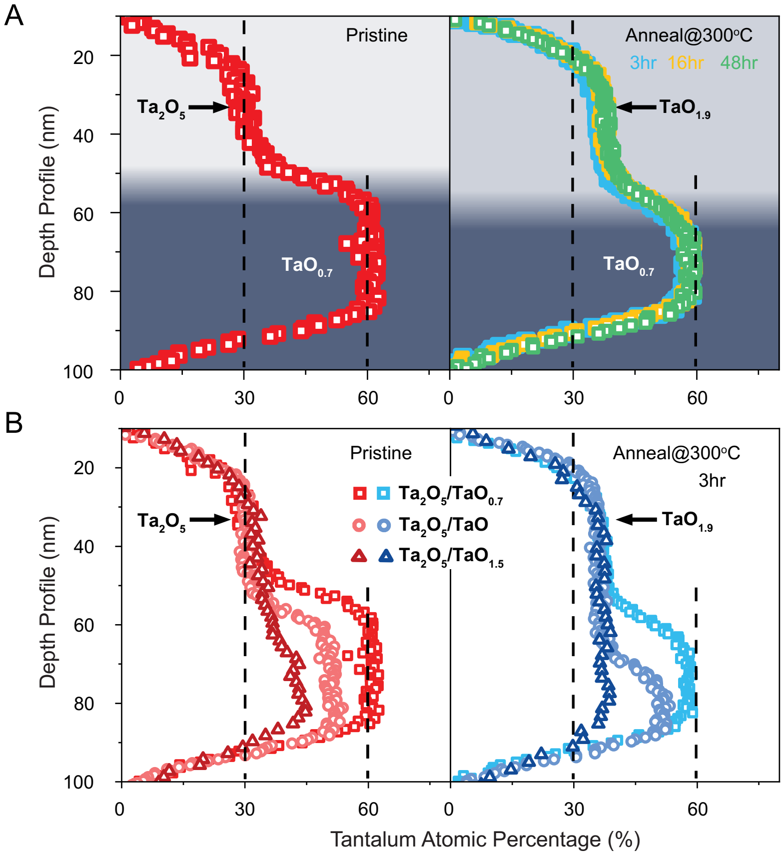

Fig. 4 Compositional phase separation probed by Auger electron spectroscopy (AES) depth profile of bilayer stack Ta_2O_5/TaO_X. a) The AES depth profile results of $Ta_2O_5/TaO_{0.7}$ before (left panel) and after annealing at 300°C for 3, 16 and 48 hours (right panel). While the Ta_2O_5 is initially oxidised to $TaO_{1.9}$, it does not undergo further exchange of oxygen with the suboxide; this persistent interface after annealing indicates compositional phase separation. A darker plot background colour indicates higher Ta content. **b)** The AES depth profile results of three bilayer stacks before (left panel) and after annealing at 300 °C for 3 hours (right panel) suggest that the solubility limit at 300°C is $TaO_{1.9}$. Our results do not show substantial sputter reduction due to the relatively uniform metal:oxygen ratio with depth within each (sub)oxide layer. Dashed vertical guidelines convey 30 at% and 60 at% Ta.

We next change the bottom suboxide to TaO and $TaO_{1.5}$. After annealing, the oxidized top layer all converts to $TaO_{1.9}$ and expands over the bottom layer while conserving oxygen (Fig. 4b). The results for all samples suggest that the $TaO_{1.9}$ sub-oxide is the solubility limit at 300°C in amorphous tantalum-oxide; this solubility limit increases to at least $TaO_{1.4}$ at 450°C (Fig. S8), consistent with an increase in the solubility for most materials at higher temperatures. In contrast, the crystalline phase diagram of tantalum oxide exhibits negligible solubility below 1000°C[43]. Even though the filament and suboxide film may possess some chemical differences, the persistent compositional interfaces (Fig. 4) and extremely stable LRS (Fig. 2) tell a consistent story: the oxygen-rich and oxygen-poor regions will not mix (Fig. 1b), but will instead remain separate (Fig. 1c). Moreover, this composition phase separation is also observed in an amorphous $HfO_2/HfO_{0.4}$ bilayer, where $HfO_{1.6}$ is measured to be a stable phase (Fig. S9). This phase separation can also explain why certain studies also show the HRS fails to the LRS in Hf-based VCM devices[28,44], like the case for Ta-based ones[15,16,20,21], despite using different combinations of top and bottom electrodes.

Ab initio thermodynamic calculations

Having experimentally shown compositional phase separation, we next investigate phase separation computationally using *ab initio* calculations and phase-field simulations. We first use density functional theory to compute the free energy of amorphous tantalum oxide across different oxygen compositions between Ta and Ta_2O_5. We use *ab initio* molecular dynamics with Canonical Ensemble (NVT) conditions, where the atomic volume is determined from the experimentally measured density (Fig. S10), to generate amorphized structures of tantalum oxide. The samples are relaxed at 0K to compute the time-averaged formation enthalpy of the amorphous phases (Fig. S11). The amorphous formation enthalpies are all higher than that of the crystalline Ta-O convex hull energies (Fig. S11); however, the crystalline states are not accessible for the temperature and times of our experiments[37] (Fig. S1).

To account for the entropy of mixing, we develop a two-sublattice model, where the configurational entropy of the oxygen sublattice is calculated from mixing between oxygen ions and vacancies, and the configurational entropy of the tantalum sublattice is calculated from the mixing between various Ta oxidation states. For the latter, we use a dynamic programming approach to solve for the number of microstates where the possible Ta oxidation states are charge-balanced by the oxygen composition (see Experimental Procedures for more details). Finally, we compute the Gibbs energy of mixing by referencing the total Gibbs free energy to that of amorphous-Ta and amorphous-Ta_2O_5 (Fig. S11). The resulting Gibbs free energy of mixing curves at T=300°C yield a 'w'-shaped curve, with the local minima located at $TaO_{1.9}$ (~35 at% Ta) and ~Ta (100 at% Ta) (Fig. 5a). These results are qualitatively consistent with previous calculations[39] that show phase separation between amorphous Ta_2O_5 and TaO_2 at 0K; however, our calculations span the entire Ta-O composition range and account for entropy.

Next, we combine the computed formation energy of amorphous tantalum oxide with a phase-field model to simulate the bilayer composition over time. In this phase-field model, mass flux (J) follows the gradient of the computed chemical potential μ from Fig. 5a and Fig. S12 via $J = -D/k_B T \, c \, \nabla\mu$, where c is the oxygen concentration and D the oxygen diffusivity. Because the crystalline Ta and Ta_2O_5 states (Fig. S11) are not kinetically accessible from the amorphous state, mass transport under the thermally-constrained metastable equilibrium will follow the chemical potential of the amorphous Ta-O compound, computed from the amorphous Gibbs Free Energy of Mixing (Fig. 5a) (see details in Experimental Procedures and Fig. S12).

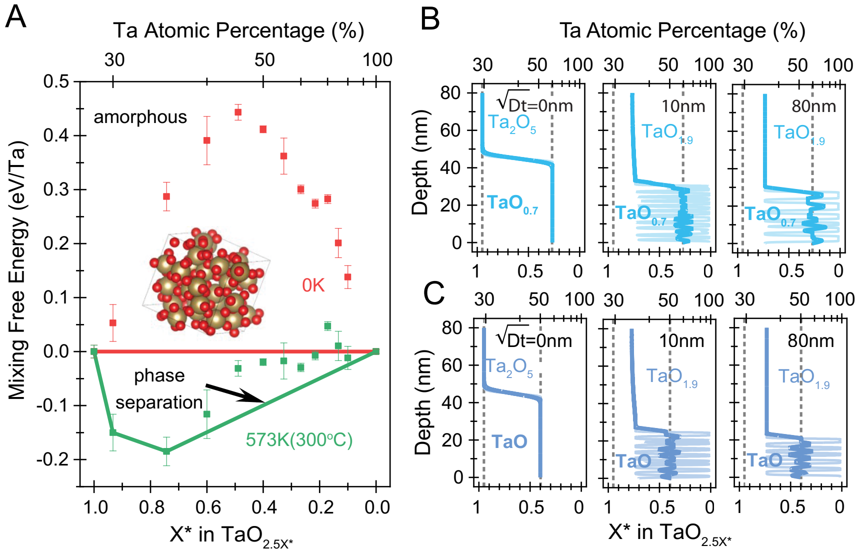

Fig. 5 Atomistic calculation and phase-field simulation of Ta-O system. a) Mixing free energy of TaO_X across a series of compositions including enthalpy and entropy at 300°C (see Experimental Procedures). These energies are referenced that of amorphous Ta (X*=0) and Ta_2O_5 (X*=1) at 0K. The common tangent and the convex hull indicate phase separation between ~$TaO_{1.9}$ (X*~0.74) and Ta (X*~0). The insert is the amorphous structure generated. **b-c)** Phase-field simulation of oxygen diffusion in bilayer stacks of (b) $Ta_2O_5/TaO_{0.7}$ and (c) Ta_2O_5/TaO which incorporates phase separation with the formation energy fitted from (a). These simulations qualitatively capture the Auger depth profile in Fig. 4b. The light color line is the simulation results, and the dark color line is the 5-nm average value to account for depth- and lateral-averaged AES measurement.

We first simulate the stacked Ta_2O_5 and sub-oxide $TaO_{0.7}$ (60 at% Ta) bilayer (Fig. 5b) in one dimension. Here, Ta_2O_5 is reduced to the solubility limit of $TaO_{1.9}$ (35 at% Ta), consistent with experiment (Fig. 4a). The bottom suboxide $TaO_{0.7}$ undergoes spinodal decomposition into two stable phases (lighter color), but the composition averaged over 5 nm remains ~$TaO_{0.7}$ (60 at% Ta). Previous electron microscopy studies of tantalum suboxide filaments have observed that they undergoes spinodal decomposition into Ta-rich and O-rich regions[42,45]. However, our 1D Auger depth profile does not have lateral resolution and only captures the average composition spatially averaged over many microns; the averaged depth profiles in Fig. 4 is consistent with a 5-nm depth-averaged simulation (darker color) in Fig. 5b. When we replace the sub-oxide layer with TaO (50 at% Ta), the top Ta_2O_5 layer is also reduced to $TaO_{1.9}$ and bottom TaO layer is decomposed into two phases with an average 50at% Ta composition (Fig. 5c), again matching experiment results (Fig. 4b). The $Ta_2O_5/TaO_{1.5}$ (40 at% Ta) bilayer simulation (Fig. S13) is again consistent with experiment (Fig. 4b), which eventually becomes a single layer with $TaO_{1.9}$ (35 at% Ta). In contrast, if we ignore phase separation and assume ideal Fickian diffusion ($J = -D\,\nabla c$), the $Ta_2O_5/TaO_{0.7}$ and Ta_2O_5/TaO bilayers evolve into a single compositionally homogeneous layer in Fig. S14, in stark contrast with experiment.

Our experimental (Fig. 4) and computational (Fig. 5) results both show persistent compositional phase separation, and independently identified the $TaO_{1.9}$ sub-oxide as one of the solubility limits at 300°C. Four-point electrical measurements show that TaO_2 is electronically insulating (Table S1) despite having a nominal 20% oxygen deficiency because it is amorphous; this result is consistent with other studies which utilize TaO_2 as the pristine, initially-insulating switching layer[42,46]; as a result, the conducting filaments must be more conducting and reside in the miscibility gap. Our results show that a film with 40at% Ta, quantified by Auger, is needed to create an electronically conducting film. This number is somewhat higher than the ones quantified in recent work using XPS (33at% Ta)[41], which we attribute to differences in the quantification values of Auger and XPS.

Phase-field simulations of device operation

Finally, we conduct 2D phase-field modeling to simulate the evolution of the conductive filament in the Ta_2O_5/TaO_X memristor over time. We consider both the ideal solid solution model that yields Fickian diffusion ($J = -D\nabla c$) used in previous work[23,47], as well as the amorphous phase separation model ($J = -D/k_B T\, c\, \nabla\mu$) based on a regular solution– details in Experimental procedures. The phase-field model here simulates mass transport under nonideal thermodynamic conditions, including but not limited to spinodal decomposition.

Substantial differences between the two models arise during retention simulations. We simulate the filament composition as $TaO_{0.4}$ based on recent transmission electron microscopy results by Skronowski and colleagues[42], and the reservoir suboxide as $TaO_{0.5}$, which is the experimentally measured suboxide composition of our devices. The ideal Fickian diffusion model shows that the pristine, LRS, and HRS will revert to the same low resistance state (Fig. S15a), like in Fig. 1a and in contrast to the pristine device results in Fig. 2. If we suppress phase separation between the two oxide layers (Fig. S15b), the pristine, LRS, and HRS will revert to the same HRS after annealing like the scheme in Fig. 1b, again contradicting the LRS measured in Fig. 2. In contrast, the regular solution model based on the calculated Gibbs free energy (Fig. S15c) shows that both the pristine and the LRS states are stable and will not fail, while the HRS state will fail and revert to LRS, all consistent with experiment (Fig. 2). In Fig. S16 and S17, we incorporated a composition-dependent oxygen diffusivity into our model. While the magnitudes and paths differ, the overall trend is essentially identical to what was observed with a composition-independent oxygen diffusivity. This results because the final state of the system is ultimately governed by thermodynamics: changing the magnitude and shape of diffusivity can change the time and path needed to reach this final state, but it cannot change the final form.

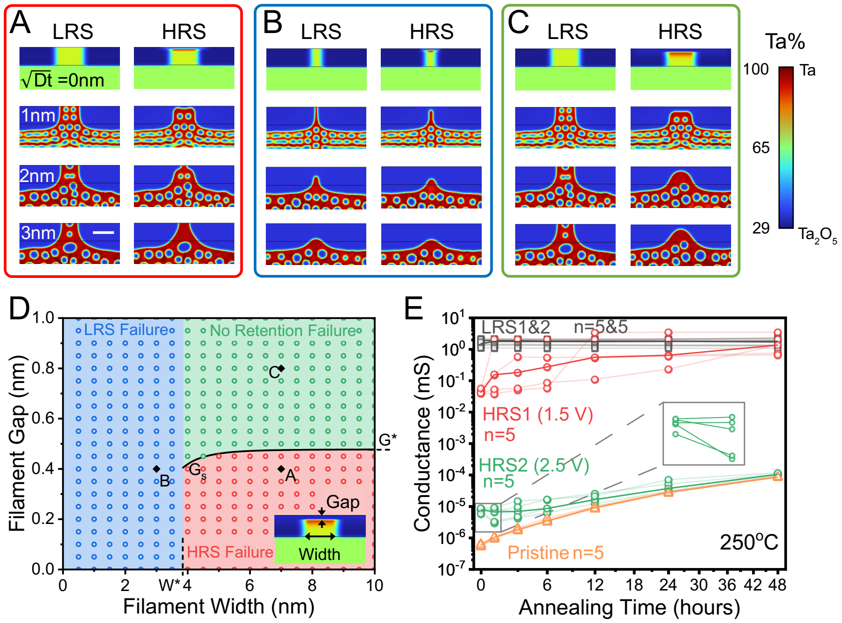

Fig. 6 Origin of HRS and LRS Retention Failure with 2D Phase field model for Ta_2O_5/$TaO_{0.5}$ bilayer memristor. a-c) Retention simulation on LRS and HRS with different filament gap and filament width. Scale bar is 5 nm. d) The simulated stability of LRS and HRS as functions of the filament width and gap. Each circle represents one simulation that maps to the schematic shown in a, b, or c. e) The experimental retention results at 250 °C using different RESET voltage (1.5 and 2.5 V). The inset shows a decrease in the HRS conductance upon baking for one hour, consistent with the predictions of (c), before increasing as a result of the increased conductance of the pristine devices (Fig. 2b).

While these simulation conditions are consistent with our experiments in Fig. 2, other researchers have shown LRS retention failure where devices revert to high resistance[14,17,18]. By parametrically exploring this phase-field model, we identify the filament width, filament gap, and gradient energy penalty as the critical parameters to assess the stability of the LRS and the HRS. Fig. 6a shows a case where the HRS fails while the LRS is stable (does not fail), which qualitatively resembles our experimental results (Fig. 2). When the filament width is decreased from 7 nm to 3.5 nm (Fig. 6b), the filament would dissolve over time, resulting in LRS retention failure[14,17,18]. Finally, by increasing the gap distance from 0.4 to 0.8 nm while keeping the filament width at 7 nm, both the LRS and HRS devices remain stable in respective states for very long times due to phase separation. We will experimentally validate these three regimes in the next section. In all cases, our phase separation model ensures that the pristine devices are insulating, like in Fig. S15c, without the need to additionally constrain transport between the reservoir and switching layers. These simulations also show the filament and suboxide layer initially separate into amorphous Ta and $TaO_{\sim1.9}$ regions with a domain size ~2 nm as a result of the solubility limits calculated in Fig. 5. These spinodal decomposition features are consistent with recent electron microscopy by Skowronski and colleagues[42,45,48].

Fig. 6d plots the retention stability range of LRS and HRS as a function of the filament width and filament gap. The critical filament width W* approximately defines the boundary between filament dissolution and strengthening, which controls whether the LRS fails. When the gap is smaller than the threshold G_s (black line), a broken filament will re-form, leading to HRS retention failure. On the other hand, when the gap is larger than the threshold G_s, the broken filament will dissolve, resulting in neither LRS nor HRS retention failure (Fig. 6c). In Fig. S18, we simulate how the critical filament width and gap are affected by the gradient energy penalty, which represents the interfacial energy. These simulations suggest that both thresholds are related to the characteristic stability wavelength λ, and provide a design rule: lowering the gradient energy penalty would increase the parameter space for the "green" stable regime given by Fig. 6c, where neither the LRS nor the HRS will fail. While the exact thresholds depend on material parameters like the gradient energy penalty (Fig. S18), the directional trends among the three failure regimes have been consistently simulated and, as we show in the next section, experimentally verified.

Experimental verification of phase-field model

Based on our predictions from Fig. 6, we experimentally identified the transition from HRS failure (red) to LRS failure (blue). Our results in Fig. S19 show that reducing the compliance current from 1 mA to 100 μA not only decreases the filament conductance, but also yields in a transition from HRS failure to LRS failure. Additional c-AFM measurements show this reduction in compliance current reduces the filament size from ~8 nm to ~3 nm (Fig. S19 c,f). The latter value (3 nm) is comparable to scalpel c-AFM images showing a ~4 nm diameter filament in a Hafnia device SET using a 50 μA compliance current[49]. These combined c-AFM and device characterization results confirm our model prediction of a transition from HRS to LRS failure with smaller filaments (Fig. 6d). In contrast, models based on Fick's First Law would suggest that larger filaments dissolve slower due to longer diffusion lengths, not the observed dichotomy in the direction of failure in our experiments.

Next, to experimentally obtain the predicted "green" region without retention failure, we used a larger RESET voltage of 2.5V (Fig. S20). These 2.5V RESET devices (HRS2) have ~4 orders of magnitude higher resistance than the 1.5V RESET devices (HRS1) on the same die. Based on previous research, this vast increase in the filament resistance most likely results from an increase in the filament gap[50]. Using the Simmons equation[51] with a barrier height of 1.5 eV, a filament diameter of 8 nm, and an electron effective mass of 1, we estimate from the measured HRS resistance that the filament gap increased from ~0.4 nm to ~0.9 nm upon increasing the RESET voltage from 1.5 to 2.5V (Fig. S21). We note that these estimates are based on idealized planar barriers, which do not account for deep traps as well as non-planar barrier shapes; additionally, while the Simmons equation may not be physically realistic for tunnel gaps <0.5 nm, the experimentally measured decrease in conductance upon a 2.5V RESET (Fig. 6e) should correspond to an increase in the tunnel gap. After 1 hour baking at 250 °C, the HRS2 devices showed a decrease in conductance, qualitatively consistent with the predictions in Fig 6c whereby the gap increases over time. Over 48 hours, the conductance of the HRS2 devices converges with that of the pristine devices, again consistent with the predictions in Fig. 6c. In contrast, the resistances of the HRS1 devices will converge with the LRS, consistent with Fig. 6a. While the longer retention times may not outweigh the higher switching voltages, our results do provide strong experimental evidence for our phase-field model.

Finally, we generalize our findings to Hafnia VCM devices made using a 65-nm process on a 300-mm wafer (see Note S1). These devices again showed a clear transition between LRS failure to HRS failure upon changing the compliance current (Fig. S22), with essentially identical statistics as the TaOx devices (Table S2). This shows that our key results are generalizable to other VCM devices, including ones made using 300 mm wafer processing tools. The "no failure" regime was not achieved because these devices would SET in a different direction upon applying -2V (Fig. S23), likely due to the TiN metallic electrode. All of the conclusions in this section are statistically significant at a Z-value > 3, p-value <0.2% (Note S1).

Discussion and Conclusions

We utilized a multimodal approach combining device measurements, scanning probe microscopy, depth profiling, *ab initio*, and continuum simulations. In conjunction, our results provide a consistent picture showing the strong consequence of phase separation on mass transport in TaOx. Our inclusion of compositional phase separation into oxygen transport models is a paradigm change for resistive memory and more broadly for defect-rich electronics. We thereby correct a longstanding and pervasive assumption of ideal solid solution used in previous physical models based on ideal Fickian diffusion[14–18,22–24]. The Fickian diffusion equation $J = -D \nabla c$ is a special case of mass transport where the mobile chemical species form an ideal thermodynamic solution with the host (Note S3). Because most binary metal-oxygen phase diagrams show phase separation for temperatures <500°C, the ideal solution assumption for $J = -D \nabla c$ is not fulfilled outside dilute limits in most crystalline metal oxides. Ideal Fickian diffusion should not be automatically assumed for filament-based VCM. However, we expect the exact Gibbs energy profile, solubility limit, and diffusion properties to be dependent on the switching oxide materials used a particular device.

Additionally, our ability to measure sub-oxide tracer diffusion (Fig. 3) and characterize composition phase separation (Fig. 4,5) reconciles vast discrepancies regarding both the magnitude and direction of retention time in TaOx VCM. While phase separation into Ta-rich and O-rich domains have previously been observed in pioneering electron microscopy measurements of the filament[42,45,48], our work explains how phase separation affects mass transport and ultimately controls the ability of memristive devices to attain a core functionality, which is to retain information over time. Although our work was conducted at elevated temperatures to accelerate oxygen diffusion, we expect the overall trends to persist at lower temperatures. However, based on the retention time exceeding 10 years at 85C, the timescales would be too long for this experiment. The composition phase separation mechanisms described in this work differ from the role of the decomposed SrO phase in $SrTiO_3$, which acts as a kinetic oxygen diffusion barrier[52]. We show that information retention in valence change memory has a thermodynamic origin–phase separation–and is not only a consequence of oxygen diffusion kinetics. While our experiments simulate oxygen, the computed chemical potential of Ta is also nonmonotonic with composition (Fig. S12d); therefore, we expect qualitatively similar diffusion characteristics if Ta is the mobile ion, as suggested in several recent experiments[42,53].

From a technological point of view, our results demonstrate that phase separation, even for metastable amorphous materials, may enable resistive switching devices with retention times unconstrained by diffusion times (Fig. 6). This design rule may be particularly important for unconventional memristors such as those made from transition metal dichalcogenides[5] and organic materials[54] that often have worse retention than TaOx and HfOx memristors. Phase separation also provides an avenue to improve retention in non-filamentary interfacial memristors[55] and electrochemical random access memory[56] (ECRAM), which has more reliable switching but poorer retention.

Beyond resistive memory, our work has broad implications for future electronics enabled by defects and defect migration. For example, oxygen vacancy migration is directly linked to ferroelectricity in orthorhombic Hafnia[2]. While the dilute point defects in traditional covalent semiconductors generally follow ideal solution thermodynamics, our work shows that this assumption may not apply to newer classes of electronic and quantum materials with much higher point defect concentrations[2–5]. Accounting for nonideal interactions including compositional phase separation is critical, and ignoring such effects can lead to substantial errors.

Experimental Procedures

Resource Availability

Lead Contact: Further information and requests for resources and reagents should be directed to and will be fulfilled by the lead contact, Yiyang Li (yiyangli@umich.edu)

Materials Availability: No new materials or reagents were generated in this work.

Data and Code Availability: The data and code for this work are available in Materials Commons at https://doi.org/10.13011/m3-n4fy-kr26. Any additional information required to reanalyze the data reported in this paper is available from the lead contact upon request.

Preparation of TaOx bilayer VCM devices

The VCM devices in this work have a cross-point area of ~1.5 × 1.5 μm^2 and are fabricated on SiO_2 (500 nm)/Si substrates in the Lurie Nanofabrication Facility (LNF) at the University of Michigan, following our previous work[47]. First, a 35 nm bottom Pd electrode with 5 nm NiCr adhesion layer is deposited by photolithography (1500/4000 rpm PMGI SF6/SPR220-3 μm photoresist with GCA AS200 AutoStep), electron beam evaporation (Angstrom Engineering Evovac Evaporator), and lift-off processes (Remover PG and Isopropanol). Next, a 30 nm $TaO_{0.5}$ reservoir layer is deposited by direct current (DC) reactive sputtering with a Kurt J. Lesker Lab 18 system using a 51 mm diameter Ta metal target, a power of 200 W for 150s, and a setpoint temperature of 400°C. The sputter pressure was 5 mTorr, and the gas was an Ar/O_2 mixture at a ratio of 32:1. Next, the sputter chamber was cooled to room temperature, and a 4 nm Ta_2O_5 switching layer is then deposited by radio frequency (RF) sputtering using a 51 mm diameter Ta_2O_5 target in Ar gas with a pressure of ~5 mTorr and a power of 30 W for 1059s. A 30/30 nm Au/Pd top electrode is then deposited by photolithography, e-beam evaporation, and lift-off processes. This top electrode also acts as a hard etch mask for the two tantalum oxide layers. A reactive ion etching process using SF_6 (Plasmatherm 790) is used to etch the two tantalum oxide layers to expose the bottom contacts. A third photolithography process is used to deposit a larger (150 by 150 μm^2), 200/10 nm Au/Ni pad by electron beam evaporation, which is used to contact the probe station.

Preparation of HfOx in-line VCM devices

The characterized HfO_2 RRAM devices were fabricated at the Albany NanoTech Complex by NY CREATES and the College of Nanotechnology, Science & Engineering of the University at Albany. The integration is based on a 65nm backend of line (BEOL) process technology with custom modules embedding the ReRAM elements between tungsten and copper metallization 1 and 2, respectively (W-M1 and Cu-M2). The W-M1 interconnect is utilized to fabricate in-line resistors with ranges from 0 to 50 kΩ enabling on-chip current overshoot control during the ReRAM forming process. An inert TiN bottom electrode (BE) was subtractively structured above the W-M1 layer with a device diameter of 80 nm for the devices characterized and shown here. The fabrication of the BE module was finished by a CMP process leaving an atomically flat contact for the deposition of the ReRAM stack. The 5.8 nm HfO_2 switching layer (SL) was deposited via atomic layer deposition (ALD) and followed by 6 and 40 nm of Ti and TiN, via physical vapor deposition (PVD), serving as the oxygen exchange layer (OEL) and top electrode (TE), respectively. The RRAM stack was structured via a reactive ion etch (RIE) process to isolate the devices and an overlay of the SL, OEL and TE above the BE of around 50 nm is maintained to avoid RIE edge effects during filament formation. The connection to the TE and W-M1 layer was accomplished via a via-first dual damascene process where the via etch and hard mask thickness is tuned to enable the bridging of the vertical height difference to connect the TiN top electrode and the W-M1 with a single patterning process. After the conclusion of the dual damascene Cu-M2 process the devices can be measured in a 1 RRAM (1R) or 1 resistor 1 RRAM (1R1R) configuration with RRAM device diameters ranging from 50 to 250 nm. The final structure can be seen in Fig. S22 for a device with an 80 nm bottom electrode.

Electrical measurements

The TaOx devices were characterized using a Keithley 4200 semiconductor parameter analyzer with a probe station. The voltage is applied to the top electrode and the bottom electrode is grounded during electrical measurements. A compliance current of 1 mA (or 0.1 mA) and -5 V stop voltage was set during electroforming. After electroforming, we switch the device 20 times between the high-resistance and low-resistance states by I-V sweeps (Fig. 2a). After this process, we SET some devices on the die into the LRS, while we RESET others into the HRS. The pristine devices did not undergo any electroforming, setting, or resetting. Fig. S2 shows switching statistics. The die was annealed in an Everbeing CG-196 environmentally-controlled probe station under ~ 300 Torr of ultra-high purity Ar (Fig. S24). No electrical measurements were taken at elevated temperatures.

After cooling the device to room temperature, the sample was taken out of the environmental chamber. We measured the conductance of each device sequentially by sweeping the voltage from 0 to 0.1 V with a sweep of 0.02 V with the Keithley 4200 in a two-probe measurement configuration. The measurements include the total device resistance, including both the bulk and contact resistance. Each die was only annealed at one temperature; because it was annealed and cooled several times, and the total annealing time is recorded.

We recognize that our anneal-and-cool approach can only resolve the hour that the device fails. In contrast, measuring the resistance during annealing at high temperatures would substantially improve the temporal resolution. However, we used anneal-and-cool because it enables us to measure many devices on a single die, providing more information about distribution and statistics; additionally, by applying all electrical measurements at room temperature, we reduce the risk that the measurements would change the device resistance due to electric fields and/or Joule heating at the filament.

To confirm that our two-point measurement setup had minimal series resistance, we placed both probes on the top electrode (Pd or W) and swept the voltage from 0 to 0.1V. For TaOx devices, the average series resistance across 10 electrodes is 3.99 Ohm with a standard deviation of 0.03 Ohm. For HfOx devices, the average series resistance was 20.63 Ohm with a standard deviation of 0.06 Ohm. This series resistance plays a minimal contribution to the measured device resistance, which is on the order of 1000 Ohm or larger. This series resistance in this measurement includes the resistance of the wires and the contact resistance between the probe and the metal electrode. This resistance does not include the contact resistance between the top metal electrode and the Ta_2O_5 or HfO_2 switching layer, which is an important factor in determining the device resistance and cannot be independently measured.

Conductive atomic force microscopy

The Au/Pd top electrode of TaO_X VCM is removed by 9 min Ar ion beam sputtering with an AJA Orion-8 Sputter System at room temperature. The gas pressure was 5 mTorr while the RF power was 50 W. The etching time is estimated by the etch rate of Au/Pd is ~7 nm/s and that of Ta_2O_5 ~2 nm/min.

The conductive AFM was done using the NT-MDT Ntegra Prima microscope with platinum-coated tips (MikroMasch, HQ:CSC37/Pt) and diamond-coated tips (Nanosensors, DT-NCHR), operated in contact mode. The conductive tip was grounded while the sample was biased with a constant voltage (0.5 V) through the conductive bottom electrode. The topography information and the current value were tracked simultaneously for constructing the electric current mapping.

For all samples, we initially scan a $(3\ \mu m)^2$ area with 256 × 256 pixels with a constant 0.5V. This enables us to localize the filaments in the LRS and HRS samples. To measure the size of the filament, we then conduct a $(500\ nm)^2$ scan area around the filament with 256 × 256 pixels with 0.5V. The diameter of filaments are determined by counting the total number of pixels with a current higher than 1nA under a circular assumption in the $(500\ nm)^2$ scan area measurement. Each pixel is taken to equal $(1.95\ nm)^2$.

Transmission Electron Microscopy

STEM measurements at the University of Michigan were taken using a Thermo Fisher Talos F200X G2, a 200 kV FEG scanning transmission electron microscope operated in STEM mode. The Velox software was used for STEM images and EDS data acquisitions. The TEM specimen was prepared using a Thermo-Fisher Helios 650 Xe Plasma FIB. The final beam condition was set at 12 keV 10 pA for the liftout polishing.

X-ray Diffraction and Reflectivity

XRD and XRR measurements were conducted using a Rigaku Smartlab X-ray diffractometer using a Cu K-α source. XRD samples were measured using a 2θ scan. The samples consist of thin films of single layer or bilayer TaO_X or HfO_X deposited on silicon.

Auger Electron Spectroscopy

Ta_2O_5/TaO_X bilayer (~35/45 nm) samples for the Auger electron spectroscopy (AES) were deposited using DC reactive sputtering using a 76 mm Ta metal target (Plasmaterials, 99.95% purity) with an AJA Orion-8 Sputter System at room temperature. The gas pressure was 5 mTorr while the power was 100 W for all depositions. The oxygen concentration X is controlled by the $Ar:O_2$ ratio in the sputtering chamber. The total gas flow rate was 40 sccm. Supplementary Table S1 shows the effects of different $Ar:O_2$ ratio in the sputter chamber on the Ta:O ratios measured in the films using AES. Annealing was conducted in ~300 Torr of Argon at elevated temperatures in the Everbeing C-196 Probe Station. Fig. S1a shows that these thin films will remain amorphous after annealing.

$HfO_2/HfO_{0.4}$ bilayer (~35/35 nm) samples were deposited using DC reactive sputtering using a 76 mm Hf metal target (AJA International Inc, 99.9% purity) with an AJA Orion-8 Sputter System at room temperature The gas pressure was 5 mTorr while the power was 100 W for all depositions. HfO_2 and $HfO_{0.4}$ layers were grown with 1:1 (50% O_2) and 397:3 (0.75% O_2) $Ar:O_2$ ratio, respectively. The total gas flow rate was 40 sccm. Annealing was conducted in ~300 Torr of Argon at 300°C in the Everbeing C-196 Probe Station. All Pt layers are also DC sputtered at 100W on a 51-mm Pt target at an Ar gas pressure of 5 mTorr. Fig. S25 confirms that these HfO_X samples will also remain amorphous after the annealing conditions.

The elemental composition of the TaO_x samples (Fig. 4) was characterized via AES using a Phi 680 scanning Auger nanoprobe from Physical Electronics (Chanhassen, MN) at Ford Research (Dearborn, MI). Data was collected using a 10 kV, 10 nA electron beam from an ~ 20 μm^2 area. Sputter depth profiling with a 2 kV argon ion gun was employed to characterize the thin film chemistry. Sputter depth was calibrated using a 100 nm SiO_2 standard sample. Our films do not show substantial sputter reduction due to the uniform Ta:O ratio with depth within each layer (Fig. 4).

Additional AES characterization of additional TaOx samples (Fig. S8) and the HfOx samples (Fig. S9) was performed at Sandia National Laboratories (Livermore, CA) using a Phi 680 scanning Auger nanoprobe from Physical Electronics (Chanhassen, MN). Data was collected using a 5 kV, 10 nA electron beam from a ~ 625 μm^2 area. Sputter depth profiling with a 2 kV Ar ion gun was employed to characterize the layered composition of each sample.

Time-of-Flight, Secondary Ion Mass Spectrometry

The $Ta^{16}O_X/Ta^{18}O_X/Ta^{16}O_X$ trilayer (~30 nm each) samples used for ToF-SIMS analysis were also grown using the AJA Orion-8 with the same target, power, and gas pressure. All three layers used the same $Ar:O_2$ ratio: Ta_2O_5 used 1:1 ratio of $Ar:O_2$; $TaO_{1.5}$ used 20:1 ratio; $TaO_{0.7}$ used 65:1 ratio. While the top and bottom layers used natural abundance oxygen (~99.8% $^{16}O_2$), the middle $Ta^{18}O_X$ layer was enriched with 99% $^{18}O_2$ (Sigma-Aldrich). The enriched Ta_2O_5 layers used 1:9 ratio of natural to $^{18}O_2$-enriched gas; the enriched $TaO_{1.5}$ used 1:1 ratio of natural to $^{18}O_2$-enriched gas; the enriched $TaO_{0.7}$ layer used 100% $^{18}O_2$-enriched gas. This approach minimizes the use of $^{18}O_2$ to reduce cost. A protective Pt film (~20 nm) is also sputtered above and below the trilayer. The films are annealed at different temperatures in the Everbeing C-196 Probe Station under Ar to initiate tracer (self) diffusion.

The ToF-SIMS measurements for the Ta_2O_5 samples were conducted using a PHI Model Thrift IV from Physical Electronics (Chanhassen, MN) at Ford Research (Dearborn, MI). Samples were analysed using a 30 kV Au+ primary ion beam over a 300 µm × 300 µm area for chemical analysis. Negative ion spectra were acquired without charge compensation. Depth profiling was executed using a 2 kV Argon sputter gun rastered over a 500 µm × 500 µm area. Data acquisition times were limited to ensure the data was collected under static SIMS conditions.

The ToF-SIMS measurements for the two suboxides ($TaO_{1.5}$, $TaO_{0.7}$) were conducted using ToF.SIMS.5-NSC instrument (ION.TOF Gmb) at Oak Ridge National Laboratory. Bi^{3+} liquid metal ion gun operating at 30 keV energy, 0.5 nA current (DC mode) and spot size ~120 nm was used as a primary source for chemical analysis. It was complemented by Cs^+ sputter ion gun operating at 1 keV energy and ~70 nA current for depth profiling and low energy electron flood gun for charge compensation. The measurements were carried out at non-interlaced mode, where each analysis scan by Bi^{3+} (100×100 µm) was followed by 2 s of sputtering with Cs^+ (300 × 300 µm). Secondary ions were analyzed by time-of-flight mass analyzers with mass resolution $m/\Delta m = 100 - 300$.

The 18O tracer concentration was computed by dividing the measured 18O counts by the 18O+16O counts from ToF-SIMS. The "normalization" in Fig. 3 and S7 was conducted by multiplying this fraction by 10 for Ta_2O_5, 2 for $TaO_{1.5}$, and 1 in $TaO_{0.7}$. This normalization enables easier comparison between the samples even though the 18O-enriched layer for the Ta_2O_5 and $TaO_{1.5}$ sample was only 10% and 50% enriched with $^{18}O_2$, respectively.

To obtain the tracer diffusivity *D* from the 18O tracer profile, we used the 1D solution to the diffusion equation based on the Fourier Series; this is equivalent to the solution to the 1D solution to the heat equation.

$$c(x,t) = \Sigma_n A_n \exp\left(-D\frac{\pi^2 n^2}{L^2} t\right) \cos\left(\frac{\pi n}{L} x\right)$$

The coefficients A_n can be obtained using the Fourier Transform of the "pristine" samples that not annealed, where *l* is the total thickness of the film (90 nm). We computed the coefficients for $n = 0$ to $n = 100$.

$$A_{n=0} = \frac{1}{L}\int_0^L c(x, t=0)\, dx$$

$$A_{n>1} = \frac{2}{L}\int_0^L c(x, t=0) \cos\left(\frac{\pi n}{L} x\right)\, dx$$

DFT calculation

Ab initio amorphous free energy calculations

To compute the formation enthalpies of amorphous TaO_x structures, we followed the method of Aykol et al.[57]Amorphous structures were generated by creating a random packing of atoms and subjecting them to AIMD in an NVT ensemble (T = 5000K, timestep=2 fs). We created a cubic random packing of N_{bulk} atoms, where $N_{bulk} \geq 100$ and is the smallest integer at which the given amorphous composition can be exactly represented. Atomic density at each composition was matched to experimental measurements and interpolated linearly where experimental values were not available.

Structures were heated and annealed for 5000 timesteps. Then, three to five isochronal snapshots were selected from the production runs and cooled down through AIMD to 300K, with a ΔT of ~14K/timestep, before being quenched to 0K by conjugate gradient optimization. If the original quench did not converge, another soft annealing was performed with AIMD at 300K for 300 timesteps, and then again quenched to 0K. The final formation enthalpy was determined via a static calculation of the quenched structure. The amorphous nature was confirmed both visually from the atomistic structure, and by inspection of the radial distribution function, where long-range radial correlations beyond 2nd nearest-neighbours became negligible. The number of isochronal snapshots for each composition is defined below in the parenthesis:

Ta (3); Ta_4O (4); Ta_3O (3); Ta_7O_3 (3); $Ta_{13}O_7$ (5); Ta_6O_4 (3); $Ta_{11}O_9$ (5); TaO (3); Ta_9O_{11} (4); Ta_2O_3 (3); Ta_7O_{13} (3); Ta_3O_7 (3); Ta_2O_5 (5)

Random packing was done using packmol[58]. Structures were visualized using VESTA[59]. The workflow to generate and calculate these structures was built on pymatgen[60], Fireworks[61], atomate[62], and mpmorph[57]. All first-principles thermodynamic calculations were performed with DFT using the Vienna ab initio software package (VASP)[63–66] using DFT basis cut-off energies, *k*-point densities, and other settings compliant with Materials Project standards[67] and Aykol *et al.*[57].

More details are given in the Supplemental Experimental Procedures.

Entropy calculation

We calculate the configurational entropy of amorphous tantalum oxide using the Two-Sublattice model, where there is a fully occupied cation lattice with integer Ta oxidation states spanning 0, 1+, 2+, 3+, 4+, and 5+; and there is an anion sublattice with O^{2-} and vacancies. The stoichiometry of the sublattices is constrained to the TaOx stoichiometry. The number of configurational microstates of the two sublattice model, Ω, is assessed numerically via dynamic programming. The configurational entropy is then determined from $S = k_b \ln \Omega$. More details are given in the Supplemental Experimental Procedures, Table S3, and Fig. 26.

Phase-field models

The mixing energy at 0K is fit with an enthalpy component of the regular solution model to generate a continuous and differentiable free energy curve (Fig. S12a) in the compound $TaO_{2.5X^*}$. We define this as the enthalpy H:

$$H = \Omega X^*(1 - X^*) \qquad (1)$$

where X* is the $TaO_{2.5}$ fraction in Ta and $TaO_{2.5}$ mixture, Ω is the positive enthalpy of mixing that controls the interaction between Ta and O particles. We fit $\Omega = 0.63$ eV (Fig. S12a). We conduct phase-field simulation with the variable X* in $TaO_{2.5X^*}$ so that X* spans 0 (Ta) and 1 ($TaO_{2.5}$).

The total calculated entropy in $TaO_{2.5X^*}$ is fit with a modified asymmetric entropy component of the regular solution model (Fig. S12b):

$$S = -ak_B X^* ln(X^*) - bk_B(1 - X^*)ln(1 - X^*) \qquad (2)$$

where a = 1.39, b = 9.96, to account for asymmetric feature of the entropy term as a function of X* (Fig. S12b).

The enthalpy and entropy components of free energy points in Fig.5a are fit with a modified regular solution model to generate a continuous and differentiable free energy curve (Fig. S12c). This fit is used to model homogeneous Gibbs free energy (G_h):

$$G_h = H - TS \qquad (3)$$

where H and S are defined in equation (1) and (2), and T is the temperature = 573K (300 °C). The chemical potential of oxygen (μ) is given as the slope of the free energy with respect to the $TaO_{2.5}$ fraction X* (Fig. S12d):

$$\mu(X^*) = \frac{\partial G_h}{\partial X*} \cdot \frac{1}{2.5} - \kappa \nabla^2 X^* \qquad (4)$$

where κ is the Cahn-Hilliard gradient energy coefficient related to the interface thickness (0.01eV/nm^2). The derivative of homogeneous Gibbs free energy (G_h) with regard to X* is divided by the number of oxygen atoms in a formula unit (2.5) to obtain the chemical potential μ of an oxygen atom. Our chemical potential uses a regular solution model that only accounts for the mixing enthalpy, entropy, and gradient energy penalty; these features were sufficient to model our experimental results. Additional features like valence variation and coupled anion-cation diffusion could be incorporated into the chemical potential when needed to model other experimental observations.

This chemical potential of oxygen (μ) is used to simulate the oxygen flux:

$$J = -\frac{D}{k_B T} c \nabla \mu \tag{5}$$

where J is the oxygen flux, D is the diffusivity of oxygen, $k_B$is Boltzmann constant, T is the temperature = 300 °C, and c is oxygen concentration that equals c_0X^*, where c_0 is the oxygen concentration in $TaO_{2.5}$. To simplify the calculations, we neglect the volume change associated with adding oxygen into $TaO_{2.5X^*}$[42].

The initial state of the 1D phase-field model is set the same as the experimental AES bilayer samples with a 35 nm Ta_2O_5 layer (X* = 0.95) and a 45 nm suboxide TaO_X layer (X = 0.7, 1, 1.5 or X* = 0.28, 0.4, 0.6). The simple Fickian diffusion model describes the oxygen flux within the concentration gradient following Fick's first law $J = -D\nabla c$.

The 2D phase-field model of the memristive device simulates the oxygen movement during retention measurement, which shares the same equations (1-5) and formation energy function (Fig.5a, S11) with our 1D phase-field model. The initial condition of the 2D model is based on the device in Fig. 2 with a 4 nm near-stoichiometric Ta_2O_5 switching layer (X* = 0.95) and a 30 nm $TaO_{0.5}$ reservoir layer (X* = 0.2). The filament spans the switching layer in the LRS and contains a gap in the HRS. We assume the conductive filament has the composition of $TaO_{0.4}$ (X* = 0.16)[42]. More details about the geometry are given in the Supplemental Experimental Procedures and Fig. S27. To minimize the number of assumptions, all of the physical parameters in our model were taken from the geometry of our device, previously published work, or our *ab initio* simulations. The only exception is the gradient energy penalty κ, which was chosen arbitrarily; however, we conducted simulations for many values of κ, and the effects of changing κ are plotted in Fig. S18. Despite Joule heating during switching, we assume the filaments remain amorphous, which is consistent with electron microscopy studies[36,42,45] as well as electro-thermal models[23,47] which show device temperatures below 500°C.

Equations are self-consistently solved using the finite element method based on the platform of COMSOL Multiphysics 6.0.2. More details are given in the Supplemental Experimental Procedures and Fig. S27.

Acknowledgments

The work by J.L., B.R., D.S., and Y.L. at the University of Michigan was supported by the National Science Foundation (NSF) under Grant no. ECCS-2106225 and startup funding from the University of Michigan College of Engineering. Y.L. acknowledges the support of an Intel Rising Star Gift. W. L. and S. Y. were supported by NSF under Grant no. CCF-1900675. The computational work by A.A. and W.S. was supported by the U.S. Department of Energy (DOE), Office of Science, Basic Energy Sciences (BES), under Award #DE-SC0021130. This research also used resources of the National Energy Research Scientific Computing Center (NERSC), a U.S. Department of Energy Office of Science User Facility located at Lawrence Berkeley National Laboratory, operated under Contract No. DE-AC02-05CH11231 using NERSC award BES-ERCAP0020148. The authors also acknowledge the Texas Advanced Computing Center (TACC) at The University of Texas at Austin for providing HPC resources that have contributed to the research results reported within this paper.

The work at Sandia National Laboratories was supported by the Laboratory-Directed Research and Development (LDRD) program. Sandia National Laboratories is a multi-mission laboratory managed and operated by National Technology and Engineering Solutions of Sandia, LLC, a wholly-owned subsidiary of Honeywell International Inc., for the U.S. Department of Energy's National Nuclear Security Administration under contract DE-NA-0003525. A.A.T., P.M., O.P., and A.V.I. was partly supported by the DOE Office of Science Research Program for Microelectronics Codesign (sponsored by ASCR, BES, HEP, NP, and FES) through the Abisko Project, PM Robinson Pino (ASCR). This paper describes objective technical results and analysis. Any subjective views or opinions that might be expressed in the paper do not necessarily represent the views of the U.S. Department of Energy or the United States Government.

The work at the University at Albany was supported by the Air Force Research Laboratory under agreement numbers FA8750-21-1-1018 and FA8750-21-1-1019. The U.S. Government may reproduce and distribute reprints for Governmental purposes, despite any copyright notation. The views and conclusions expressed herein are solely those of the authors and do not necessarily reflect the official policies or endorsements of the Air Force Research Laboratory or the U.S. Government.

The authors acknowledge the Michigan Center for Materials Characterization for use of the instruments and staff assistance. Fabrication of the RRAM devices was conducted at the University of Michigan Lurie Nanofabrication Facility. A part of the ToF-SIMS measurements was conducted at the Center for Nanophase Materials Sciences, which is a DOE Office of Science User Facility, and using instrumentation within ORNL's Materials Characterization Core provided by UT-Battelle, LLC under Contract No. DE-AC05-00OR22725 with the U.S. Department of Energy.

Finally, we thank Christoph Baumer (University of Twente), Elliot J. Fuller (Sandia National Labs), and Ilia Valov & Stephan Menzel (Juelich Research Centre) for helpful discussions and feedback.

Captions

References

1. Pantelides, S.T. (1978). The electronic structure of impurities and other point defects in semiconductors. Rev. Mod. Phys. *50*, 797–858. https://doi.org/10.1103/RevModPhys.50.797.

2. Nukala, P., Ahmadi, M., Wei, Y., de Graaf, S., Stylianidis, E., Chakrabortty, T., Matzen, S., Zandbergen, H.W., Björling, A., Mannix, D., et al. (2021). Reversible oxygen migration and phase transitions in hafnia-based ferroelectric devices. Science *372*, 630–635. https://doi.org/10.1126/science.abf3789.

3. Zhao, Y., Yavuz, I., Wang, M., Weber, M.H., Xu, M., Lee, J.-H., Tan, S., Huang, T., Meng, D., Wang, R., et al. (2022). Suppressing ion migration in metal halide perovskite via interstitial doping with a trace amount of multivalent cations. Nat. Mater. *21*, 1396–1402. https://doi.org/10.1038/s41563-022-01390-3.

4. Zhang, Z., Zuo, F., Wan, C., Dutta, A., Kim, J., Rensberg, J., Nawrodt, R., Park, H.H., Larrabee, T.J., Guan, X., et al. (2017). Evolution of Metallicity in Vanadium Dioxide by Creation of Oxygen Vacancies. Phys. Rev. Applied *7*, 034008. https://doi.org/10.1103/PhysRevApplied.7.034008.

5. Sangwan, V.K., Liu, S.E., Trivedi, A.R., and Hersam, M.C. (2022). Two-dimensional materials for bio-realistic neuronal computing networks. Matter *5*, 4133–4152. https://doi.org/10.1016/j.matt.2022.10.017.

6. Waser, R., Dittmann, R., Staikov, G., and Szot, K. (2009). Redox-Based Resistive Switching Memories - Nanoionic Mechanisms, Prospects, and Challenges. Adv. Mater. *21*, 2632–2663. https://doi.org/10.1002/adma.200900375.

7. Yang, J.J., Strukov, D.B., and Stewart, D.R. (2013). Memristive devices for computing. Nature Nanotech *8*, 13–24. https://doi.org/10.1038/nnano.2012.240.

8. Ielmini, D., and Wong, H.-S.P. (2018). In-memory computing with resistive switching devices. Nat Electron *1*, 333–343. https://doi.org/10.1038/s41928-018-0092-2.

9. Xia, Q., and Yang, J.J. (2019). Publisher Correction: Memristive crossbar arrays for brain-inspired computing. Nat. Mater. *18*, 518–518. https://doi.org/10.1038/s41563-019-0357-9.

10. Dittmann, R., Menzel, S., and Waser, R. (2022). Nanoionic memristive phenomena in metal oxides: the valence change mechanism. Advances in Physics *70*, 155–349. https://doi.org/10.1080/00018732.2022.2084006.

11. Yang, Y., Zhang, X., Qin, L., Zeng, Q., Qiu, X., and Huang, R. (2017). Probing nanoscale oxygen ion motion in memristive systems. Nat Commun *8*, 15173. https://doi.org/10.1038/ncomms15173.

12. Kwon, D.-H., Kim, K.M., Jang, J.H., Jeon, J.M., Lee, M.H., Kim, G.H., Li, X.-S., Park, G.-S., Lee, B., Han, S., et al. (2010). Atomic structure of conducting nanofilaments in TiO2 resistive switching memory. Nature Nanotech *5*, 148–153. https://doi.org/10.1038/nnano.2009.456.

13. Larentis, S., Cagli, C., Nardi, F., and Ielmini, D. (2011). Filament diffusion model for simulating reset and retention processes in RRAM. Microelectronic Engineering *88*, 1119–1123. https://doi.org/10.1016/j.mee.2011.03.055.

14. Choi, S., Lee, J., Kim, S., and Lu, W.D. (2014). Retention failure analysis of metal-oxide based resistive memory. Appl. Phys. Lett. *105*, 113510. https://doi.org/10.1063/1.4896154.

15. Wei, Z., Takagi, T., Kanzawa, Y., Katoh, Y., Ninomiya, T., Kawai, K., Muraoka, S., Mitani, S., Katayama, K., Fujii, S., et al. (2011). Demonstration of high-density ReRAM ensuring 10-year retention at 85°C based on a newly developed reliability model. In 2011 International Electron Devices Meeting, p. 31.4.1-31.4.4. https://doi.org/10.1109/IEDM.2011.6131650.

16. Park, J., Choi, J., Kim, G., Kim, G., Kim, G.S., Song, H., Kim, Y.S., Lee, Y., Rhee, H., Lee, H.M., et al. (2022). Modified Dynamic Physical Model of Valence Change Mechanism Memristors. ACS Appl. Mater. Interfaces *14*, 35949–35958. https://doi.org/10.1021/acsami.2c10944.

17. Chen, Y.Y., Goux, L., Clima, S., Govoreanu, B., Degraeve, R., Kar, G.S., Fantini, A., Groeseneken, G., Wouters, D.J., and Jurczak, M. (2013). Endurance/Retention Trade-off on HfO_2/Metal Cap 1T1R Bipolar RRAM. IEEE Transactions on Electron Devices *60*, 1114–1121. https://doi.org/10.1109/TED.2013.2241064.

18. Azzaz, M., Vianello, E., Sklenard, B., Blaise, P., Roule, A., Sabbione, C., Bernasconi, S., Charpin, C., Cagli, C., Jalaguier, E., et al. (2016). Endurance/Retention Trade Off in HfOx and TaOx Based RRAM. In 2016 IEEE 8th International Memory Workshop (IMW), pp. 1–4. https://doi.org/10.1109/IMW.2016.7495268.

19. Ueki, M., Hayashi, Y., Furutake, N., Masuzaki, K., Tanabe, A., Narihiro, M., Sunamura, H., Uejima, K., Mitsuiki, A., Takeda, K., et al. (2017). Stabilizing Schemes for the Minority Failure Bits in Ta2O5-Based ReRAM Macro. IEEE Transactions on Electron Devices *64*, 419–426. https://doi.org/10.1109/TED.2016.2639283.

20. Goux, L., Fantini, A., Chen, Y.Y., Redolfi, A., Degraeve, R., and Jurczak, M. (2014). Evidences of Electrode-Controlled Retention Properties in Ta2O5-Based Resistive-Switching Memory Cells. ECS Solid State Letters *3*, Q79–Q81. https://doi.org/10.1149/2.0011412ssl.

21. Kim, W., Wouters, D.J., Menzel, S., Rodenbücher, C., Waser, R., and Rana, V. (2016). Lowering forming voltage and forming-free behavior of Ta2O5 ReRAM devices. In 2016 46th European Solid-State Device Research Conference (ESSDERC), pp. 164–167. https://doi.org/10.1109/ESSDERC.2016.7599612.

22. Kumar, S., Wang, Z., Huang, X., Kumari, N., Davila, N., Strachan, J.P., Vine, D., Kilcoyne, A.L.D., Nishi, Y., and Williams, R.S. (2016). Conduction Channel Formation and Dissolution

Due to Oxygen Thermophoresis/Diffusion in Hafnium Oxide Memristors. ACS Nano *10*, 11205–11210. https://doi.org/10.1021/acsnano.6b06275.

23. Kim, S., Choi, S., and Lu, W. (2014). Comprehensive Physical Model of Dynamic Resistive Switching in an Oxide Memristor. ACS Nano *8*, 2369–2376. https://doi.org/10.1021/nn405827t.

24. Larentis, S., Nardi, F., Balatti, S., Gilmer, D.C., and Ielmini, D. (2012). Resistive Switching by Voltage-Driven Ion Migration in Bipolar RRAM—Part II: Modeling. IEEE Transactions on Electron Devices *59*, 2468–2475. https://doi.org/10.1109/TED.2012.2202320.

25. Torre, C.L. (2019). Physics-Based Compact Modeling of Valence-Change-Based Resistive Switching Devices.

26. Lee, J., Schell, W., Zhu, X., Kioupakis, E., and Lu, W.D. (2019). Charge Transition of Oxygen Vacancies during Resistive Switching in Oxide-Based RRAM. ACS Appl. Mater. Interfaces *11*, 11579–11586. https://doi.org/10.1021/acsami.8b18386.

27. Lee, M.-J., Lee, C.B., Lee, D., Lee, S.R., Chang, M., Hur, J.H., Kim, Y.-B., Kim, C.-J., Seo, D.H., Seo, S., et al. (2011). A fast, high-endurance and scalable non-volatile memory device made from asymmetric Ta2O(5-x)/TaO(2-x) bilayer structures. Nat Mater *10*, 625–630. https://doi.org/10.1038/nmat3070.

28. Jiang, H., Han, L., Lin, P., Wang, Z., Jang, M.H., Wu, Q., Barnell, M., Yang, J.J., Xin, H.L., and Xia, Q. (2016). Sub-10 nm Ta Channel Responsible for Superior Performance of a HfO2 Memristor. Sci Rep *6*, 28525. https://doi.org/10.1038/srep28525.

29. Cahn, J.W., and Hilliard, J.E. (1958). Free Energy of a Nonuniform System. I. Interfacial Free Energy. The Journal of Chemical Physics *28*, 258–267.

30. Funck, C., and Menzel, S. (2021). Comprehensive Model of Electron Conduction in Oxide-Based Memristive Devices. ACS Appl. Electron. Mater. *3*, 3674–3692. https://doi.org/10.1021/acsaelm.1c00398.

31. Zhao, M., Wu, H., Gao, B., Zhang, Q., Wu, W., Wang, S., Xi, Y., Wu, D., Deng, N., Yu, S., et al. (2017). Investigation of statistical retention of filamentary analog RRAM for neuromophic computing. In 2017 IEEE International Electron Devices Meeting (IEDM), p. 39.4.1-39.4.4. https://doi.org/10.1109/IEDM.2017.8268522.

32. Nakamura, R., Toda, T., Tsukui, S., Tane, M., Ishimaru, M., Suzuki, T., and Nakajima, H. (2014). Diffusion of oxygen in amorphous Al2O3, Ta2O5, and Nb2O5. Journal of Applied Physics *116*, 033504. https://doi.org/10.1063/1.4889800.

33. Shin, D. (2024). Data for Oxygen Tracer Diffusion in Amorphous Hafnia Films for Resistive Memory. (Materials Commons). https://doi.org/10.13011/m3-e9jr-6g69 https://doi.org/10.13011/m3-e9jr-6g69.

34. Wei, Z., Kanzawa, Y., Arita, K., Katoh, Y., Kawai, K., Muraoka, S., Mitani, S., Fujii, S., Katayama, K., Iijima, M., et al. (2008). Highly reliable TaOx ReRAM and direct evidence of

redox reaction mechanism. In 2008 IEEE International Electron Devices Meeting, pp. 1–4. https://doi.org/10.1109/IEDM.2008.4796676.

35. Schie, M., Marchewka, A., Müller, T., Souza, R.A.D., and Waser, R. (2012). Molecular dynamics simulations of oxygen vacancy diffusion in SrTiO3. J. Phys.: Condens. Matter *24*, 485002. https://doi.org/10.1088/0953-8984/24/48/485002.

36. Park, G.-S., Kim, Y.B., Park, S.Y., Li, X.S., Heo, S., Lee, M.-J., Chang, M., Kwon, J.H., Kim, M., Chung, U.-I., et al. (2013). In situ observation of filamentary conducting channels in an asymmetric Ta2O5−x/TaO2−x bilayer structure. Nat Commun *4*, 2382. https://doi.org/10.1038/ncomms3382.

37. Ezhilvalavan, S., and Tseng, T.Y. (1999). Preparation and properties of tantalum pentoxide (Ta2O5) thin films for ultra large scale integrated circuits (ULSIs) application – A review. Journal of Materials Science: Materials in Electronics *10*, 9–31. https://doi.org/10.1023/A:1008970922635.

38. Miao, F., Strachan, J.P., Yang, J.J., Zhang, M.-X., Goldfarb, I., Torrezan, A.C., Eschbach, P., Kelley, R.D., Medeiros-Ribeiro, G., and Williams, R.S. (2011). Anatomy of a Nanoscale Conduction Channel Reveals the Mechanism of a High-Performance Memristor. Advanced Materials *23*, 5633–5640. https://doi.org/10.1002/adma.201103379.

39. Yang, J.J., Zhang, M.-X., Strachan, J.P., Miao, F., Pickett, M.D., Kelley, R.D., Medeiros-Ribeiro, G., and Williams, R.S. (2010). High switching endurance in TaOx memristive devices. Applied Physics Letters *97*, 232102. https://doi.org/10.1063/1.3524521.

40. Pedersen, C.S., Chang, J.H., Li, Y., Pryds, N., and Garcia Lastra, J.M. (2020). Phase separation in amorphous tantalum oxide from first principles. APL Materials *8*, 071108. https://doi.org/10.1063/5.0011390.

41. Heisig, T., Lange, K., Gutsche, A., Goß, K.T., Hambsch, S., Locatelli, A., Menteş, T.O., Genuzio, F., Menzel, S., and Dittmann, R. Chemical Structure of Conductive Filaments in Tantalum Oxide Memristive Devices and Its Implications for the Formation Mechanism. Advanced Electronic Materials, 2100936. https://doi.org/10.1002/aelm.202100936.

42. Ma, Y., Goodwill, J.M., Li, D., Cullen, D.A., Poplawsky, J.D., More, K.L., Bain, J.A., and Skowronski, M. (2019). Stable Metallic Enrichment in Conductive Filaments in TaO-Based Resistive Switches Arising from Competing Diffusive Fluxes. Advanced Electronic Materials *5*, 1800954. https://doi.org/10.1002/aelm.201800954.

43. Garg, S.P., Krishnamurthy, N., Awasthi, A., and Venkatraman, M. (1996). The O-Ta (Oxygen-Tantalum) system. JPE *17*, 63–77. https://doi.org/10.1007/BF02648373.

44. Fang, Z., Yu, H.Y., Liu, W.J., Wang, Z.R., Tran, X.A., Gao, B., and Kang, J.F. (2010). Temperature Instability of Resistive Switching on \hboxHfO_x-Based RRAM Devices. IEEE Electron Device Letters *31*, 476–478. https://doi.org/10.1109/LED.2010.2041893.

45. Ma, Y., Li, D., Herzing, A.A., Cullen, D.A., Sneed, B.T., More, K.L., Nuhfer, N.T., Bain, J.A., and Skowronski, M. (2018). Formation of the Conducting Filament in TaOx-Resistive Switching Devices by Thermal-Gradient-Induced Cation Accumulation. ACS Appl. Mater. Interfaces *10*, 23187–23197. https://doi.org/10.1021/acsami.8b03726.

46. Kim, M., Rehman, M.A., Lee, D., Wang, Y., Lim, D.-H., Khan, M.F., Choi, H., Shao, Q.Y., Suh, J., Lee, H.-S., et al. (2022). Filamentary and Interface-Type Memristors Based on Tantalum Oxide for Energy-Efficient Neuromorphic Hardware. ACS Appl. Mater. Interfaces *14*, 44561–44571. https://doi.org/10.1021/acsami.2c12296.

47. Lee, S.H., Moon, J., Jeong, Y., Lee, J., Li, X., Wu, H., and Lu, W.D. (2020). Quantitative, Dynamic TaOx Memristor/Resistive Random Access Memory Model. ACS Appl. Electron. Mater. *2*, 701–709. https://doi.org/10.1021/acsaelm.9b00792.

48. Skowronski, M. (2023). Material instabilities in the TaOx-based resistive switching devices (Invited). In 2023 IEEE International Reliability Physics Symposium (IRPS), pp. 1–5. https://doi.org/10.1109/IRPS48203.2023.10117796.

49. Celano, U., Goux, L., Degraeve, R., Fantini, A., Richard, O., Bender, H., Jurczak, M., and Vandervorst, W. (2015). Imaging the Three-Dimensional Conductive Channel in Filamentary-Based Oxide Resistive Switching Memory. Nano Lett. *15*, 7970–7975. https://doi.org/10.1021/acs.nanolett.5b03078.

50. Ielmini, D., and Menzel, S. (2016). Universal Switching Behavior. In Resistive Switching (John Wiley & Sons, Ltd), pp. 317–340. https://doi.org/10.1002/9783527680870.ch11.

51. Simmons, J.G. (1963). Generalized Formula for the Electric Tunnel Effect between Similar Electrodes Separated by a Thin Insulating Film. Journal of Applied Physics *34*, 1793–1803. https://doi.org/10.1063/1.1702682.

52. Baeumer, C., Schmitz, C., Ramadan, A.H.H., Du, H., Skaja, K., Feyer, V., Müller, P., Arndt, B., Jia, C.-L., Mayer, J., et al. (2015). Spectromicroscopic insights for rational design of redox-based memristive devices. Nat Commun *6*, 8610. https://doi.org/10.1038/ncomms9610.

53. Wedig, A., Luebben, M., Cho, D.-Y., Moors, M., Skaja, K., Rana, V., Hasegawa, T., Adepalli, K.K., Yildiz, B., Waser, R., et al. (2016). Nanoscale cation motion in TaOx, HfOx and TiOx memristive systems. Nature Nanotech *11*, 67–74. https://doi.org/10.1038/nnano.2015.221.

54. Yuan, L., Liu, S., Chen, W., Fan, F., and Liu, G. (2021). Organic Memory and Memristors: From Mechanisms, Materials to Devices. Advanced Electronic Materials *7*, 2100432. https://doi.org/10.1002/aelm.202100432.

55. Correll, J.M., Bothra, V., Cai, F., Lim, Y., Lee, S.H., Lee, S., Lu, W.D., Zhang, Z., and Flynn, M.P. (2020). A Fully Integrated Reprogrammable CMOS-RRAM Compute-in-Memory Coprocessor for Neuromorphic Applications. IEEE Journal on Exploratory Solid-State Computational Devices and Circuits *6*, 36–44. https://doi.org/10.1109/JXCDC.2020.2992228.

56. Kim, D.S., Watkins, V.J., Cline, L.A., Li, J., Sun, K., Sugar, J.D., Fuller, E.J., Talin, A.A., and Li, Y. (2023). Nonvolatile Electrochemical Random-Access Memory under Short Circuit. Advanced Electronic Materials *9*, 2200958. https://doi.org/10.1002/aelm.202200958.

57. Aykol, M., Dwaraknath, S.S., Sun, W., and Persson, K.A. (2018). Thermodynamic limit for synthesis of metastable inorganic materials. Science Advances *4*, eaaq0148. https://doi.org/10.1126/sciadv.aaq0148.

58. Martínez, L., Andrade, R., Birgin, E.G., and Martínez, J.M. (2009). PACKMOL: A package for building initial configurations for molecular dynamics simulations. Journal of Computational Chemistry *30*, 2157–2164. https://doi.org/10.1002/jcc.21224.

59. Momma, K., and Izumi, F. (2011). VESTA 3 for three-dimensional visualization of crystal, volumetric and morphology data. J Appl Cryst *44*, 1272–1276. https://doi.org/10.1107/S0021889811038970.

60. Ong, S.P., Richards, W.D., Jain, A., Hautier, G., Kocher, M., Cholia, S., Gunter, D., Chevrier, V.L., Persson, K.A., and Ceder, G. (2013). Python Materials Genomics (pymatgen): A robust, open-source python library for materials analysis. Computational Materials Science *68*, 314–319. https://doi.org/10.1016/j.commatsci.2012.10.028.

61. Jain, A., Ong, S.P., Chen, W., Medasani, B., Qu, X., Kocher, M., Brafman, M., Petretto, G., Rignanese, G.-M., Hautier, G., et al. (2015). FireWorks: a dynamic workflow system designed for high-throughput applications. Concurrency and Computation: Practice and Experience *27*, 5037–5059. https://doi.org/10.1002/cpe.3505.

62. Mathew, K., Montoya, J.H., Faghaninia, A., Dwarakanath, S., Aykol, M., Tang, H., Chu, I., Smidt, T., Bocklund, B., Horton, M., et al. (2017). Atomate: A high-level interface to generate, execute, and analyze computational materials science workflows. Computational Materials Science *139*, 140–152. https://doi.org/10.1016/j.commatsci.2017.07.030.

63. Kresse, G., and Hafner, J. (1993). Ab initio molecular dynamics for liquid metals. Phys. Rev. B *47*, 558–561. https://doi.org/10.1103/PhysRevB.47.558.

64. Kresse, G., and Hafner, J. (1994). Ab initio molecular-dynamics simulation of the liquid-metal--amorphous-semiconductor transition in germanium. Phys. Rev. B *49*, 14251–14269. https://doi.org/10.1103/PhysRevB.49.14251.

65. Kresse, G., and Furthmüller, J. (1996). Efficiency of ab-initio total energy calculations for metals and semiconductors using a plane-wave basis set. Computational Materials Science *6*, 15–50. https://doi.org/10.1016/0927-0256(96)00008-0.

66. Kresse, G., and Furthmüller, J. (1996). Efficient iterative schemes for ab initio total-energy calculations using a plane-wave basis set. Phys. Rev. B *54*, 11169–11186. https://doi.org/10.1103/PhysRevB.54.11169.

67. Jain, A., Ong, S.P., Hautier, G., Chen, W., Richards, W.D., Dacek, S., Cholia, S., Gunter, D., Skinner, D., Ceder, G., et al. (2013). Commentary: The Materials Project: A materials genome

approach to accelerating materials innovation. APL Materials *1*, 011002. https://doi.org/10.1063/1.4812323.

Author Contributions

J.L. and Y.L. conceived the experiment and analyzed the experimental data. J.L. measured RRAM device performance, prepared all materials characterization samples for the TaO_X samples, and conducted the X-ray measurements. D. S. prepared the HfO_X samples. J.L. and S.Y. fabricated RRAM devices. J.L. and B.R. performed the phase field simulations. A.A. and W.S. conducted the DFT and entropy calculations. S.L.P., R.H., and A.A.T. performed the AES measurements. J.L., T.C., O.P., and P.M. performed conductive atomic force microscopy. E.T.H. and A.V.I. performed the ToF-SIMS measurements. K.S. performed transmission electron microscopy. Y.L. supervised the project. All authors contributed to data interpretation and writing the text.

Conflicts of Interest

The authors declare no competing interests.